Geophysical Journal International

Geophys. J. Int. (2016) **206,** 1424–1430
Advance Access publication 2016 June 8
GJI Seismology

doi: 10.1093/gji/ggw218

Aftershock seismicity and tectonic setting of the 2015 September 16 M_w 8.3 Illapel earthquake, Central Chile

Dietrich Lange,[1] Jacob Geersen,[1] Sergio Barrientos,[2] Marcos Moreno,[3] Ingo Grevemeyer,[1] Eduardo Contreras-Reyes[2] and Heidrun Kopp[1]

[1] *GEOMAR, Helmholtz Centre for Ocean Research Kiel, Wischhofstr.* 1–3, 24148 *Kiel, Germany. E-mail: dlange@geomar.de*
[2] *Departamento de Geofísica, Facultad de Ciencias Físicas y Matemáticas, Universidad de Chile, Blanco Encalada* 2002, *Santiago, Chile*
[3] *GFZ, German Research Center for Geosciences, Telegrafenberg* 1, 14473 *Potsdam, Germany*

Accepted 2016 June 6. Received 2016 May 31; in original form 2015 November 25

SUMMARY

Powerful subduction zone earthquakes rupture thousands of square kilometres along continental margins but at certain locations earthquake rupture terminates. To date, detailed knowledge of the parameters that govern seismic rupture and aftershocks is still incomplete. On 2015 September 16, the M_w 8.3 Illapel earthquake ruptured a 200 km long stretch of the Central Chilean subduction zone, triggering a tsunami and causing significant damage. Here, we analyse the temporal and spatial pattern of the coseismic rupture and aftershocks in relation to the tectonic setting in the earthquake area. Aftershocks cluster around the area of maximum coseismic slip, in particular in lateral and downdip direction. During the first 24 hr after the main shock, aftershocks migrated in both lateral directions with velocities of approximately 2.5 and 5 km hr^{-1}. At the southern rupture boundary, aftershocks cluster around individual subducted seamounts that are related to the downthrusting Juan Fernández Ridge. In the northern part of the rupture area, aftershocks separate into an upper cluster (above 25 km depth) and a lower cluster (below 35 km depth). This dual seismic–aseismic transition in downdip direction is also observed in the interseismic period suggesting that it may represent a persistent feature for the Central Chilean subduction zone.

Key words: Earthquake dynamics; Seismicity and tectonics; Subduction zone processes; Continental margins: convergent; Dynamics: seismotectonics; South America.

1 INTRODUCTION

On 2015 September 16, the M_w 8.3 Illapel earthquake (Ye *et al.* 2016) ruptured a 200 km long stretch of the Central Chilean subduction zone (Fig. 1). The 2015 Illapel earthquake occurred in a segment of the subduction zone that last ruptured in an M_w 8.3 earthquake in 1943 (Beck *et al.* 1998). From its magnitude, areal extent and associated tsunami, the 2015 earthquake seems to mimic the 1943 event (inlay, Fig. 1). Prior to 1943, the area experienced large earthquakes on 1880 August 15, 1730 July 8 and possibly 1647 May 13 (Beck *et al.* 1998) but the size and magnitude of the historic events are not well defined. The area to the south of the 2015 Illapel earthquake experienced M_w. 7.8 earthquakes in 1971 and 1985 (Barrientos 1995) and an M 8.3 event in 1906 (Okal 2005), that close the gap to the northern end of the rupture area of the great 2010 M_w 8.8 Maule earthquake (e.g. Lange *et al.* 2012). Farther to the north between ∼26°S and 29°S, an M_w 8.4 earthquake on 1922 November 11 triggered a significant tsunami with run-up heights of up to 9 m along the Chilean coast (Lomnitz 2004). Here, we investigate the temporal and spatial pattern of aftershocks and coseismic rupture of the 2015 Illapel earthquake in relation to the tectonic setting. For this purpose, we combine high-resolution swath bathymetric data from a suite of research cruises with local seismicity and a coseismic slip model inverted from GPS data.

2 DATA AND METHODS

2.1 Earthquake data and relocation

We used 5.639 events recorded by a dense network of 30 land-stations between 26°S and 35°S and 28 additional stations from onshore Chile from the time period 2013 January 1–2016 February 10. After event detection, 81.598 P- and S-arrival times were manually picked from the national data set provided by the Centro Sismológico Nacional, Chile (CSN). The earthquakes were relocated with a local 1-D velocity model from the CSN optimized for Central Chile. For the location with the 1-D velocity model, we estimated station corrections (Fig. S1, Supporting Information) accounting for lateral variations in the subsurface. Station corrections

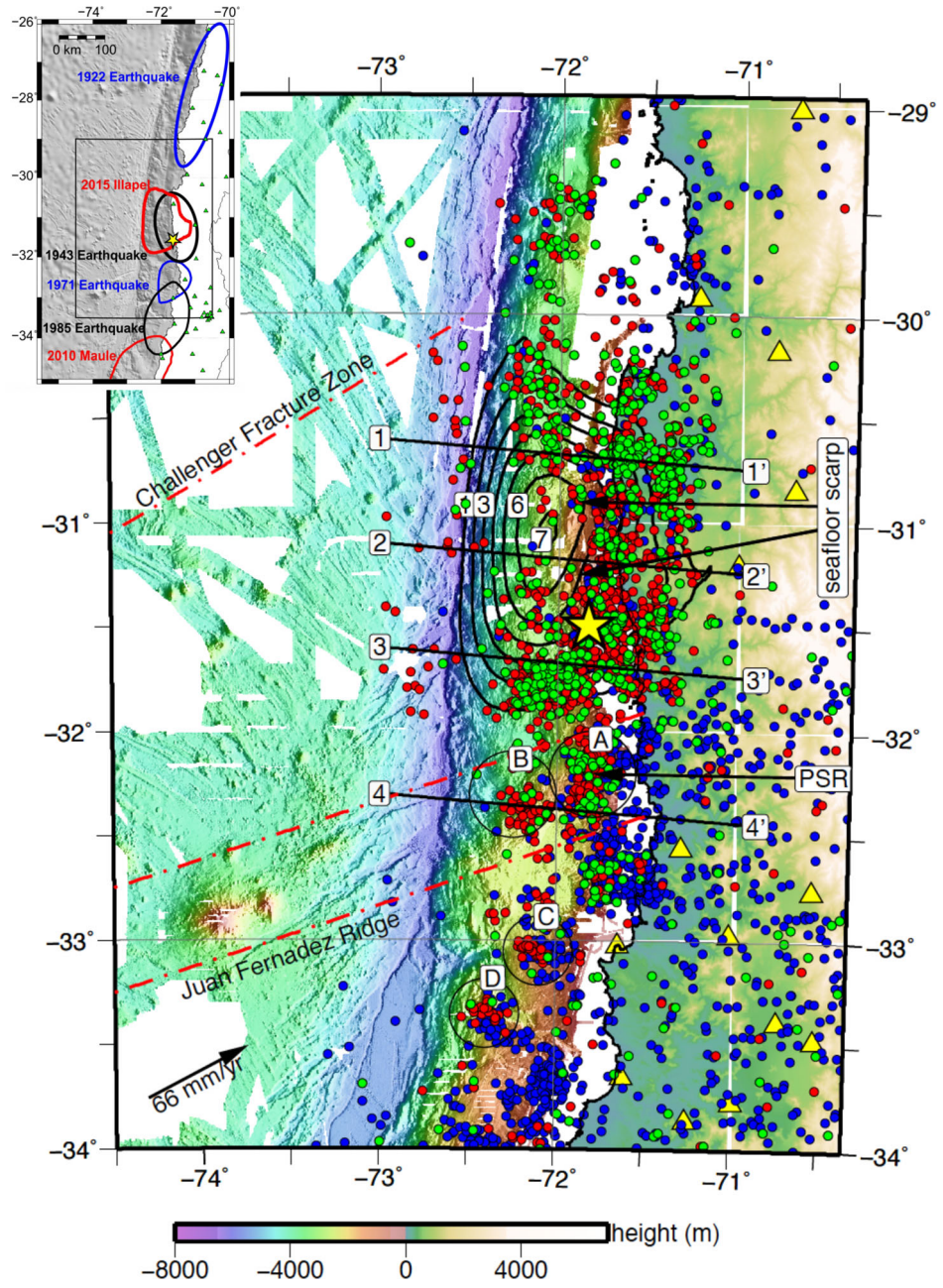

Figure 1. Map showing the coseismic slip model and the local seismicity of the M_w 8.3 2015 Illapel earthquake in relation to forearc structures. The yellow star marks the epicentre of the 2015 Illapel earthquake and black lines indicate the coseismic slip model (1 m slip contours). Blue circles indicate seismicity before the Illapel rupture starting on 2013 January 1. Red circles indicate aftershocks that occurred in the first two months after the main shock and green circles show aftershocks that occurred afterwards until 2016 February 10. Local seismicity is based on a local 1-D velocity model from the Centro Sismológico Nacional, Chile, together with station corrections (Fig. S1, Supporting Information). The two black circles labelled A and B around 32.3°S encircle clusters of aftershocks that developed around the subducting seamounts of the Juan Fernández Ridge (JFR). Cluster C corresponds to the location of the subducted San Antonio seamount (Laursen & Normark 2002) whereas no seamount has been mapped at the location of cluster D. The dashed black lines indicate the four vertical profiles shown in Fig. 2. The JFR and CFZ are indicated by red dashed lines (for details see the text). Yellow triangles indicate seismic stations. Inset map at upper left corner shows the slip areas of the 1922 earthquake, 1943 earthquake (Beck *et al.* 1998), 1971 earthquake and 1985 earthquake (Barrientos 1995) and 2015 Illapel earthquake (this study).

account for deviations from the a priori model and are determined from the average residual at each station. In areas of pre-dominate 2-D structure (such as subduction zones), the minimum 1-D velocity model with station corrections is a good approximation of the 3-D structure (e.g. Kissling 1988). We considered a subset of 3.691 earthquakes (based on more than seven onsets for 33.976 P- and 29.499 S-arrival times). Events were located with the non-linear oct-tree search algorithm (NonLinLoc; Lomax *et al.* 2000). The oct-tree algorithm provides hypocentre uncertainties by exploring the probability density functions of each individual event. The maximum likelihood location is chosen as the preferred event location.

Furthermore, in order to assess along-strike and across-strike structural heterogeneities, we constructed quasi-3-D models by transposing the east–west oriented 2-D velocity models of Moscoso *et al.* (2011) and Contreras-Reyes *et al.* (2015) across the entire study region following the geometry of the trench. The determination of hypocentre locations using the quasi-3-D velocity models resulted in overall larger rms values than the location determination using the local 1-D velocity model together with station corrections. In particular, the 3-D heterogeneities located on the onshore prolongation of the subducting Juan Fernández Ridge (JFR), such as the change from flat slab to 'normal' slab inclination, cannot be approximated with a 2-D model transposed along the trench. As a result, we use the 1-D velocity model with station corrections to account for lateral changes of the forearc structure.

2.2 Coseismic slip model of 2015 Illapel earthquake

Coseismic slip distributions of both, dip-slip and strike-slip components were estimated using a damped linear least-squares inversion using a finite-element model. The model takes into account the geometrical complexities of the Chile subduction zone (e.g. Moreno *et al.* 2009), incorporating not only the geometry of the subduction slab (Hayes *et al.* 2012) but also topography, bathymetry (Amante & Eakins 2009) and the continental Moho (Tassara & Echaurren 2012). The structure of our 3-D model consists of four blocks: continental plate, viscoelastic continental mantle, oceanic plate and viscoelastic oceanic mantle. The megathrust fault was discretized in triangular patches with an average patch size of 66 km^2. We specified a Young's modulus of 90, 120 and 160 GPa, for the continental, oceanic and mantle layers, respectively. The Poisson's ratio was set to 0.265 and 0.30 for continental and oceanic crust, respectively. All numerical simulations in this study are solved with the finite-element modelling software PyLith (Aagaard *et al.* 2013). Vertical and horizontal displacements from 18 cGPS sites (Fig. S2, Supporting Information) were inverted to produce the slip distribution of the megathrust earthquake. Positive and maximum slip (15 m) constraints were applied to avoid models with unreasonable slip patterns and to improve the model resolution. Additional constraints that taper the slip to zero along the trench were imposed at the upper fault borders.

2.3 High-resolution multibeam bathymetric data

High-resolution multibeam bathymetric data were collected during multiple seagoing campaigns lead or co-lead by GEOMAR Helmholtz Centre for Ocean Research Kiel. The database at GEOMAR combines swath bathymetric soundings from cruises carried out between 1995 and 2010 (e.g. von Huene *et al.* 1995; Flueh *et al.* 2002) and may be accessed through the Ocean Science Information System OSIS-Kiel (portal.geomar.de/osis). The data were complemented with some swath transects from the National Center for Environmental Information (NCEI) database.

3 RESULTS AND DISCUSSION

The southern boundary of aftershock seismicity during the 2015 Illapel earthquake spatially coincides with the intersection of the JFR, a ∼900 km long chain of 11 seamount groups, with the trench (Fig. 1). Landward of the trench, along the strike of the JFR, the Punta Salinas Ridge (PSR) forms a prominent topographic expression in the marine forearc that is interpreted to be caused by uplift above the underthrusting seamounts of the JFR (von Huene *et al.* 1997). The location of the PSR coincides with two circular aftershock clusters (labelled A and B, Fig. 1), with the first cluster spatially coinciding with the subducting Papudo Seamount (Yáñez *et al.* 2001). A third cluster is located at the Topocalma Knoll (around 33°S, labelled C in Fig. 1) which is presumably caused by the subduction of the large San Antonio seamount (Laursen & Normark 2002) and a fourth cluster (labelled D, Fig. 1) is observed closer to the trench at ∼33.3°S.

Subducting seamounts and variations in subducting seafloor roughness are believed to influence interplate coupling and spatial migration of earthquake rupture (e.g. Wang & Bilek 2011; Geersen *et al.* 2015). Around 32.3°S, the subducting seamounts of the JFR, cause widespread (over tens of kilometres) fracturing around the initial plate boundary fault zone. The spatial location of the aftershock clusters may be controlled by fracture networks induced by the subducting seamounts (Wang & Bilek 2011), which may well represent the cause for the increased seismicity in the area of the JFR in the interseismic period. Parallel to creating heterogeneous stresses, large subducted relief (>1000 m) creates unfavourable conditions for ruptures to propagate across (Sparkes *et al.* 2010). Therefore, the subduction of the JFR is suggested to control the southern boundary of the 2015 Illapel earthquake and the clustering of aftershocks between 32°S and 33°S.

Across the margin in updip and downdip direction, variations in seismic rupture and aftershocks correlate to first-order structural variations in the overriding South American Plate (Fig. 2). All aftershock clusters coincide with the areas of positive Coulomb stress change recently determined by Tilmann *et al.* (2016) with maximum values up to 0.2 MPa (clusters A and B). Stress transfer from the coseismic rupture during the 2015 Illapel earthquake therefore likely triggered the development of aftershock clusters A and B at ∼32°S–32.3°S and possibly also clusters C and D at ∼33°S–33.3°S. Aftershocks in the south started ∼24 hr (clusters A and B) and 72 hr (clusters C and D) after the main shock (Fig. 3). In addition to Coulomb stress changes, afterslip may be an alternative or additional triggering mechanism for the aftershocks. Aftershocks migrated southwards from the main shock to the latitude of clusters A and B at a rate of 5 km hr^{-1} for the first 24 hr (Fig. 3).

Profiles of aftershocks from the northern rupture area (Fig. 2, panels E and F) show a clear separation into an upper cluster (above 25 km depth) and a lower cluster (below 35 km depth) indicating two seismic–aseismic transitions in downdip direction. The separation of seismicity into two depth levels in the northern part of the rupture area is also observed in the two years prior to the Illapel 2015 main shock (Fig. 2, panels A and B). A similar clustering of aftershocks in two depth levels downdip of the coseismic rupture was first observed in the wake of the M_w 8.8 Maule earthquake (Lange *et al.* 2012) suggesting that the band of deep seismicity could be a general pattern for the Central Chilean subduction zone. For the Maule 2010 and the Illapel 2015 earthquakes, the depth of the aseismic region between the upper and the lower cluster roughly coincides with the depth of the continental Moho from receiver function analysis (Gilbert *et al.* 2006; Dannowski *et al.* 2013). However, beyond this observation of spatial correlation with the continental Moho, the physical processes that govern the separation of seismicity into two depth levels remains enigmatic. Alternative explanations could be dehydration processes or coupling heterogeneities of the subduction interface.

Between 30.5°S and 31.5°S, in the area of maximum coseismic slip, aftershocks occur almost exclusively landward of an N-S

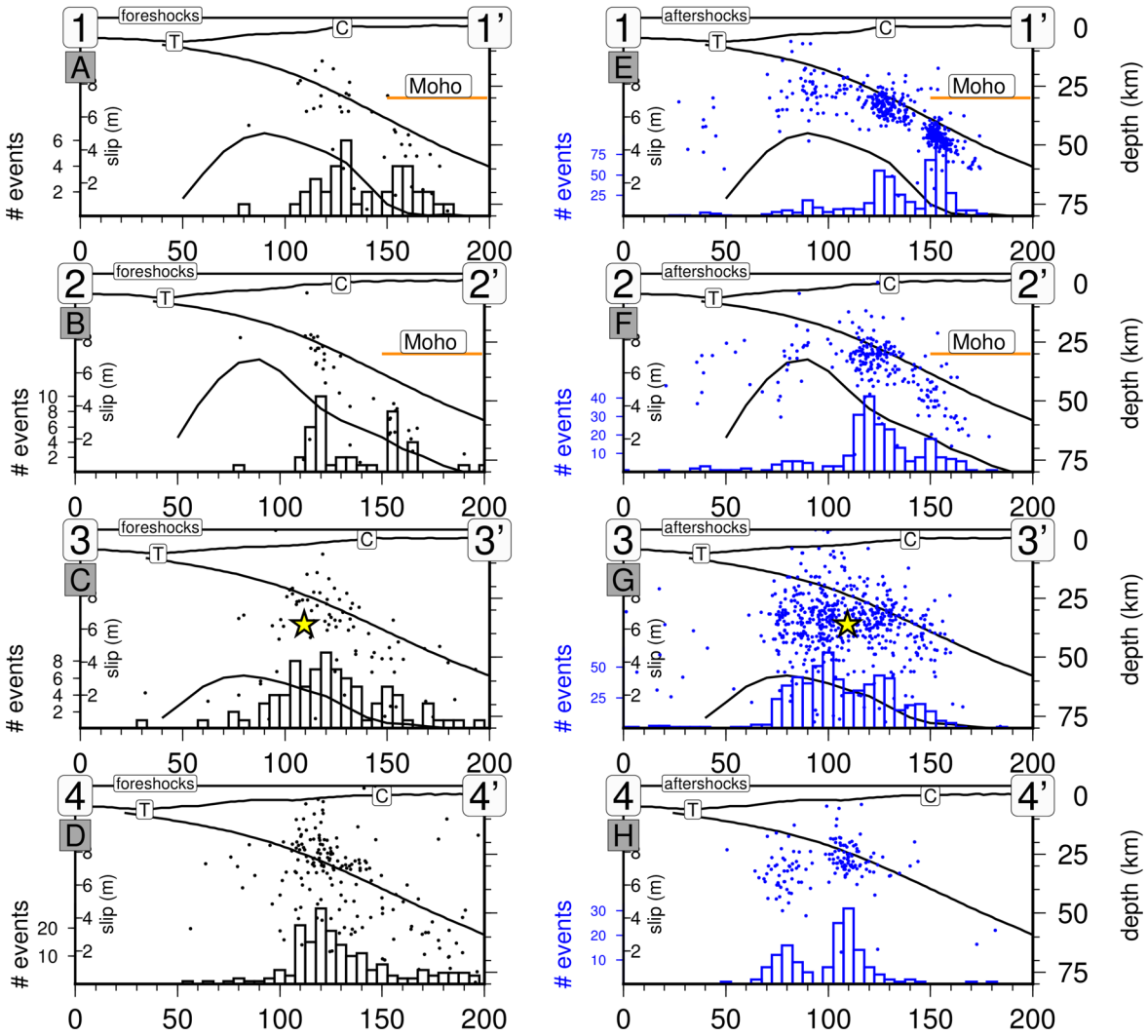

Figure 2. Trench perpendicular vertical profiles showing foreshocks (left, panels A–D) and aftershocks (right, panels E–H) of the 2015 Illapel earthquake together with a global slab model (Hayes *et al.* 2012). The histograms show the number of events along the sections together with the coseismic slip model. Events are shown within 25 km of either side of the profiles. In profiles 1 and 2, the orange line indicates the location of the continental Moho inferred from P receiver functions (Gilbert *et al.* 2006). The yellow star marks the Illapel 2015 main shock. T and C indicate the locations of the trench and the coast. Hypocentral depths of events located offshore become progressively less reliable with increasing distance from the coast and should be interpreted with caution. Profile locations are indicated in Fig. 1.

striking, steeply inclined (30°), seaward dipping seafloor escarpment (800 m seafloor offset) located at around 2000 m water depth and constituting the surface expression of a large seaward dipping normal fault (Contreras-Reyes *et al.* 2015 and Fig. 1). In contrast to the aftershocks, high slip (>4 m) during the 2015 Illapel earthquake extends farther updip into the area seaward of the large normal fault (Fig. 4). At the lower continental slope, seaward of the maximum slip patch of the 2015 Illapel earthquake and at 10–20 km distance from the deformation front, a splay fault system separates the active accretionary prism to the west from the outermost forearc block to the east (Contreras-Reyes *et al.* 2015).

The Challenger Fracture Zone (CFZ) has previously been interpreted to intersect the trench at around 30°S (e.g. Tebbens & Cande 1997; Yáñez *et al.* 2001; Tilmann *et al.* 2016) (Fig. 1). However, swath bathymetric data do not image the fracture zone as a spatially continuous morphologic feature. The region of the extrapolated trace of the CFZ based on oceanic plate ages and magnetic lineations (Yáñez *et al.* 2002; Müller *et al.* 2008) does not exhibit significant relief. In some areas (e.g. 31°S–32°S), a narrow (∼5 km) chain of elevated basement topography rising some hundreds of metres above the surrounding seafloor is observed. However, these seamounts are probably related to mid-ocean seafloor spreading rather than to a fracture zone. Farther towards the trench no distinct morphologic expression can be linked to the CFZ (Fig. 1) which could serve as a major rupture boundary after subduction.

As observed for the southern earthquake boundary, aftershocks migrate from the initial rupture area into the region north of the 2015 Illapel earthquake (Fig. 3). The rate of aftershock migration is ∼2.5 km hr^{-1} for the first 24 hr following the main shock. However, no distinct clusters of aftershocks develop in the north in contrast to the southern earthquake boundary. The lack of distinct aftershock clusters in the north further lends support to the interpretation that the northern earthquake boundary is not controlled by any large-scale structural variation, such as the subducting seamounts in the south.

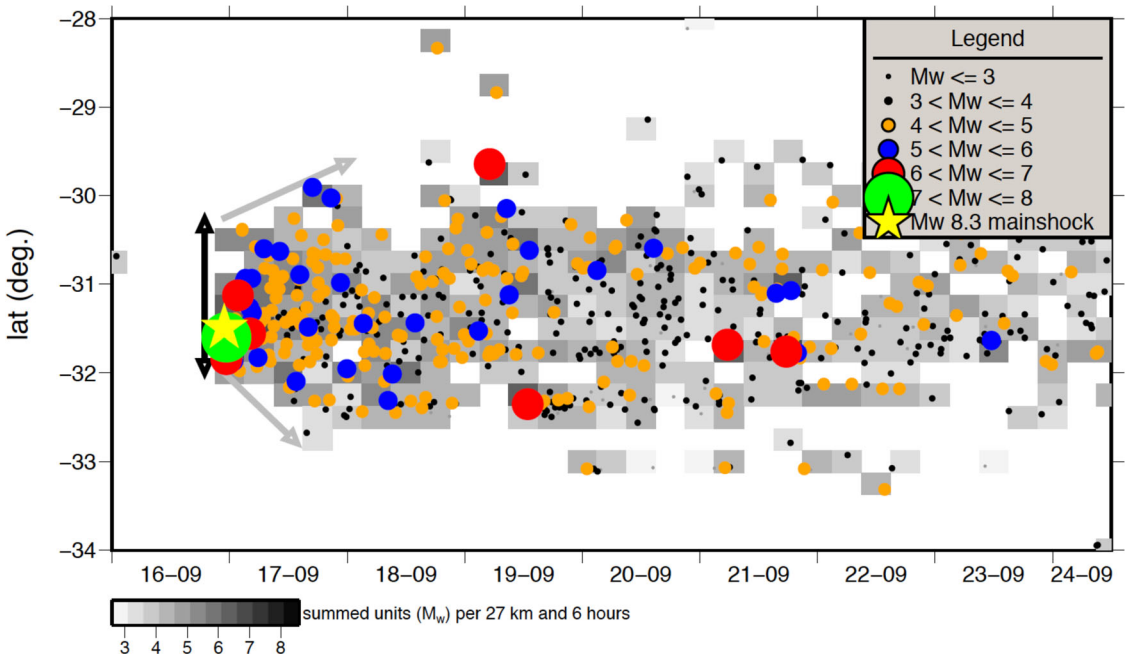

Figure 3. Temporal and lateral distribution of aftershocks for the first eight days after the Illapel 2015 main shock. From the coseismic rupture area, the aftershocks migrated in north and south direction with migration velocities of 2.5 and ∼5 km s^{-1}, respectively.

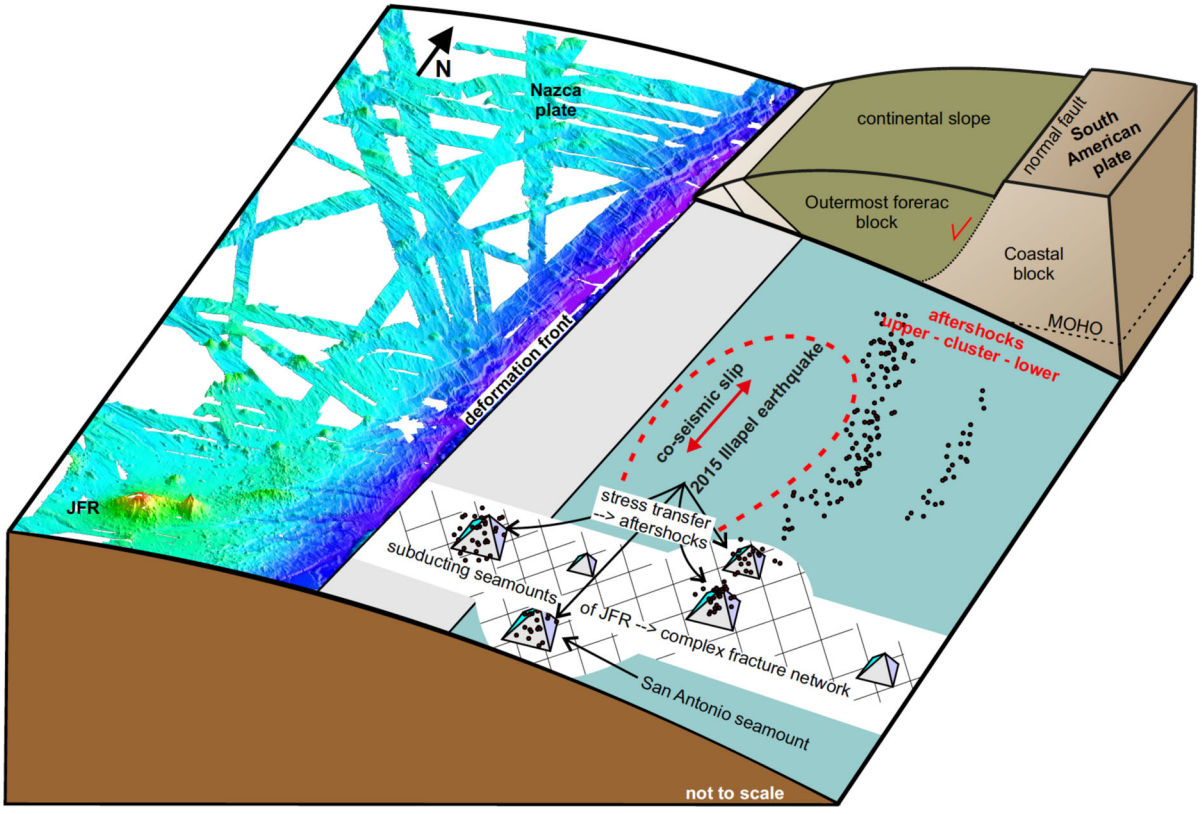

Figure 4. Cartoon summarizing the seismo-tectonic setting in the area of the 2015 Illapel earthquake.

The reason for the spatial spreading of the aftershocks, compared to the coseismic rupture, may be due to the maximum differential stress changes in the region around the rupture area (Das & Henry 2003). According to poroelastic fluid diffusion models (Miller *et al.* 2004; Terakawa *et al.* 2013), the occurrence of earthquakes can drastically change the surrounding pore fluid pressure fields. Miller *et al.* (2004) studied the 1997 Umbria–Marche seismic sequence in Italy, and proposed that aftershocks of large earthquakes may be driven by the coseismic release of trapped, highly pressurized fluids propagating through damage zones created during coseismic rupture. The associated pressure pulses are suggested to trigger aftershocks by reducing the effective normal stress of incipient slip

applies. However, aftershock migration related to fluid-driven processes was reported to be significantly smaller (<1 km s^{-1}) (Roland & McGuire 2009, and references therein) than the observed migration velocity flowing the first day after the Illapel 2015 earthquake. A further test of the viability of these or other ideas will require in-depth modelling, for example, of diffusion processes and Coulomb stress changes, beyond the scope of this study.

4 CONCLUSIONS

We discuss the tectonic setting in the area of the 2015 Illapel earthquake in relation to the coseismic rupture and the distribution of aftershocks. The southern rupture termination is suggested to be related to the subducting JFR where aftershocks cluster around subducting seamounts. In the northern part of the 2015 Illapel rupture area, aftershocks show a deep band of seismicity at 40–60 km depth. A similar deep band of seismicity is observed before the 2015 Illapel earthquake and in the aftershock series following the M_w 8.8 Maule 2010 earthquake. The observations of hypocentre distributions of the foreshocks and aftershocks of the Illapel earthquake as well as the for the aftershock series of the Maule earthquake indicate that the distribution of seismicity into two depth levels could be a persistent feature during the seismic cycle and possibly a general pattern for the Central Chilean margin. For the first day after the main shock, we observe migration of aftershocks in north and south directions with migration velocities of 2.5 and 5 km s^{-1}, respectively.

ACKNOWLEDGEMENTS

R/V SONNE Cruise SO161 was carried out with grant no. 03G0161A/B by the Bundesministerium für Bildung und Forschung (BMBF). JG was funded by a grant (CP1404) of the Cluster of Excellence 80 'The Future Ocean'. The Future Ocean is funded within the framework of the Excellence Initiative by the Deutsche Forschungsgemeinschaft (DFG) on behalf of the German federal and state governments. Local seismicity was provided by the Chilean National Seismic Network, Universidad de Chile. Event detection and phase picking was conducted at CSN. Furthermore, we used station PEL (operated by the Institute de Physique du Globe de Paris) and station LCO (operated by IRIS/USGS).

REFERENCES

Aagaard, B.T., Knepley, M.G. & Williams, C.A., 2013. A domain decomposition approach to implementing fault slip in finite-element models of quasi-static and dynamic crustal deformation, *J. geophys. Res.,* **118,** 3059–3079.

Amante, C. & Eakins, B.W., 2009. ETOPO1 1 Arc-Minute Global Relief Model: Procedures, Data Sources and Analysis. NOAA Technical Memorandum NESDIS NGDC-24. National Geophysical Data Center, NOAA, doi:10.7289/V5C8276M.

Barrientos, S.E., 1995. Dual seismogenic behavior: the 1985 Central Chile earthquake, *Geophys. Res. Lett.,* **22**(24), 3541–3544.

Beck, S., Barrientos, S., Kausel, E. & Reyes, M., 1998. Source characteristics of historic earthquakes along the central Chile subduction zone, *J. South Am. Earth Sci.,* **11.2,** 115–129.

Contreras-Reyes, E., Ruiz, J.A., Becerra, J., Kopp, H., Reichert, C., Maksymowicz, A. & Arriagada, C., 2015. Structure and tectonics of the central Chilean margin (31°–33°S): implications for subduction erosion and shallow crustal seismicity, *Geophys. J. Int.,* **203,** 776–791.

Dannowski, A., Grevemeyer, I., Kraft, H. A., Arroyo, I. & Thorwart, M., 2013. Crustal thickness and mantle wedge structure from receiver functions in the Chilean Maule region at 35°S, *Tectonophysics,* **592,** 159–164.

Das, S. & Henry, C., 2003. Spatial relation between main earthquake slip and its aftershock distribution, *Rev. Geophys.,* **41**(3), 1013, doi:10.1029/2002RG000119.

Flueh, E.R., Kopp, H. & Schreckenberger, B., eds. 2002. RV SONNE Cruise report SO161-1&4. SPOC. GEOMAR-Report, 102. GEOMAR Forschungszentrum für Marine Geowissenschaften, Kiel, 391 pp., doi:10.3289/GEOMAR_Report_102_2002.

Geersen, J., Ranero, C.R., Barckhausen, U. & Reichert, C., 2015. Subducting seamounts control interplate coupling and seismic rupture in the 2014 Iquique earthquake area, *Nat. Commun.,* **6,** 8267, doi:10.1038/ncomms9267.

Gilbert, H., Beck, S. & Zandt, G., 2006. Lithospheric and upper mantle structure of central Chile and Argentina, *Geophys. J. Int.,* **165.1,** 383–398.

Hayes, G.P., Wald, D.J. & Johnson, R.L., 2012. Slab1.0: a three-dimensional model of global subduction zone geometries, *J. geophys. Res.,* **117,** B01302, doi:10.1029/2011JB008524.

Kissling, E., 1988. Geotomography with local earthquake data, *Rev. Geophys.,* **26,** 659–698.

Lange, D. *et al.*, 2012. Aftershock seismicity of the 27 February 2010 M_w 8.8 Maule earthquake rupture zone, *Earth planet. Sci. Lett.,* **317–318,** 413–425.

Laursen, J. & Normark, W.R., 2002. Late Quaternary evolution of the San Antonio Submarine Canyon in the central Chile forearc (∼33 S), *Mar. Geol.,* **188**(3), 365–390.

Lomax, A., Virieux, J., Volant, P. & Berge, C., 2000. Probabilistic earthquake location in 3D and layered models: introduction of a Metropolis–Gibbs method and comparison with linear locations, in *Advances in Seismic Event Location*, pp. 101–134, eds Thurber, C. & Rabinowitz, N., Kluwer, Amsterdam.

Lomnitz, C., 2004. Major earthquakes of Chile: a historical survey, 1535-1960, *Seismol. Res. Lett.,* **75**(3), 368–378.

Miller, S.A., Collettini, C., Chiaraluce, L., Cocco, M., Barchi, M. & Kaus, B.J.P., 2004. Aftershocks driven by high-pressure CO_2 source at depth, *Nature,* **427,** 724–727.

Moreno, M.S., Bolte, J., Klotz, J. & Melnick, D., 2009. Impact of megathrust geometry on inversion of coseismic slip from geodetic data: application to the 1960 Chile earthquake, *Geophys. Res. Lett.,* **36,** L16310, doi:10.1029/2009GL039276.

Moscoso, E., Grevemeyer, I., Contreras-Reyes, E., Flueh, E.R., Dzierma, Y., Rabbel, W. & Thorwart, M., 2011. Revealing the deep structure and rupture plane of the 2010 Maule, Chile earthquake ($M_w = 8.8$) using wide angle seismic data, *Earth planet. Sci. Lett*., **307** (1–2), 147–155.

Müller, R.D., Sdrolias, M., Gaina, C. & Roest, W., 2008. Age, spreading rates, and spreading asymmetry of the world's ocean crust, *Geochem. Geophys. Geosyst.,* **9,** Q04006, doi:10.1029/2007GC001743.

Okal, E.A., 2005. A re-evaluation of the great Aleutian and Chilean earthquakes of 1906 August 17, *Geophys. J. Int.,* **161**(2), 268–282.

Roland, E. & McGuire, J., 2009. Earthquake swarms on transform faults, *Geophys. J. Int.,* **178,** 1677–1690.

Sparkes, R., Tilmann, F., Hovius, N. & Hillier, J., 2010. Subducted seafloor relief stops rupture in South American great earthquakes: implications for rupture behaviour in the 2010 Maule, Chile earthquake, *Earth planet. Sci. Lett.,* **298**(1–2), 89–94.

Tassara, A. & Echaurren, A., 2012. Anatomy of the Andean subduction zone: three-dimensional density model upgraded and compared against global-scale models, *Geophys. J. Int.,* **189**(1), 161–168.

Tebbens, S.F. & Cande, S.C., 1997. Southeast Pacific tectonic evolution from early Oligocene to Present, *J. geophys. Res.,* **102,** 12 061–12 084.

Terakawa, T., Hashimoto, C. & Matsu'ura, M., 2013. Changes in seismic activity following the 2011 Tohoku-Oki earthquake: effects of pore fluid pressure, *Earth planet. Sci. Lett.,* **365**, 17–24.

Tilmann, F. *et al.*, 2016. The 2015 Illapel earthquake, central Chile: a type case for a characteristic earthquake?, *Geophys. Res. Lett.,* **43,** 574–583.

von Huene, R., Corvalán, J. & Korstgard, J., 1995. Fahrtbericht zur Forschungsreise SO101–CONDOR/Cruise report SO101–CONDOR,

Valparaiso–Chile–Valparaiso, 23.03.95–08.05.95. GEOMAR Forschungszentrum für marine Geowissenschaften der Christian-Albrechts-Universität zu Kiel, *Kiel,* 177 pp., doi:10.3289/CR_SO101.

von Huene, R., Corvalán, J., Flueh, E.R., Hinz, K., Korstgard, J., Ranero, C.R. & Weinrebe, E., 1997. Tectonic control of the subducting Juan Fernández Ridge on the Andean margin near Valparaiso, Chile, *Tectonics,* **16**(3), 474–488.

Wang, K. & Bilek, S.L., 2011. Do subducting seamounts generate or stop large earthquakes?, *Geology,* **39,** 819–822.

Yáñez, G.A., Ranero, C.R., von Huene, R. & Diaz, J., 2001. Magnetic anomaly interpretation across the southern central Andes (32°–34°S): the role of the Juan Fernández Ridge in the late Tertiary evolution of the margin, *J. geophys. Res.,* **106,** 6325–6345.

Yáñez, G., Cembrano, J., Pardo, M., Ranero, C.R. & Selles, D., 2002. The Challenger-Juan Fernandez-Maipo major tectonic transition of the Nazca-Andean subduction system at 33–34°S: geodynamic evidence and implications, *J. South Am. Earth Sci.,* **15,** 23–38.

Ye, L., Lay, T., Kanamori, H. & Koper, K., 2016. Rapidly estimated seismic source parameters for the 16 September 2015 Illapel, Chile M_w 8.3 earthquake, *Pure appl. Geophys.,* **173,** 321–332.

SUPPORTING INFORMATION

Additional Supporting Information may be found in the online version of this paper:

Figure S1. P- and S-station corrections after six iterations with NonLinLoc using the 1-D velocity model of the Centro Sismológico Nacional, Universidad de Chile (CSN). The station delays account for lateral changes of the velocity structure. In particular at 32.5°S and ∼30°S strong lateral changes of station corrections are observed. The station corrections are derived from a location run using a high quality subset of 788 events with 13.543 P-arrivals and 6.485 S-arrivals.

Figure S2. Mapview showing the coseismic displacements caused by the 2015 Illapel earthquake together with the coseismic slip model. Modelled horizontal and vertical displacements indicated by blue arrows. Red arrows indicate observed geodetic displacements. The interpolated mesh shows the total slip along the curved subduction interface.
(http://gji.oxfordjournals.org/lookup/suppl/doi:10.1093/gji/ggw218/-/DC1).

Please note: Oxford University Press is not responsible for the content or functionality of any supporting materials supplied by the authors. Any queries (other than missing material) should be directed to the corresponding author for the paper.